remote sensing

Article

Estimating the Influence of Spectral and Radiometric Calibration Uncertainties on EnMAP Data Products—Examples for Ground Reflectance Retrieval and Vegetation Indices

Martin Bachmann [1],*, Aliaksei Makarau [1], Karl Segl [2] and Rudolf Richter [1]

[1] Earth Observation Center (EOC), German Aerospace Center (DLR), München Str. 20, Weßling 82234, Germany; E-Mails: aliaksei.makarau@dlr.de (A.M.); rudolf.richter@dlr.de (R.R.)

[2] Helmholtz Center Potsdam, GFZ German Research Center for Geosciences, Remote Sensing Section, Telegrafenberg A17, Potsdam 14473, Germany; E-Mail: karl.segl@gfz-potsdam.de

* Author to whom correspondence should be addressed; E-Mail: martin.bachmann@dlr.de; Tel.: +49-815-328-3325; Fax: +49-815-328-1458.

Abstract: As part of the EnMAP preparation activities this study aims at estimating the uncertainty in the EnMAP L2A ground reflectance product using the simulated scene of Barrax, Spain. This dataset is generated using the EnMAP End-to-End Simulation tool, providing a realistic scene for a well-known test area. Focus is set on the influence of the expected radiometric calibration stability and the spectral calibration stability. Using a Monte-Carlo approach for uncertainty analysis, a larger number of realisations for the radiometric and spectral calibration are generated. Next, the ATCOR atmospheric correction is conducted for the test scene for each realisation. The subsequent analysis of the generated ground reflectance products is carried out independently for the radiometric and the spectral case. Findings are that the uncertainty in the L2A product is wavelength-dependent, and, due to the coupling with the estimation of atmospheric parameters, also spatially variable over the scene. To further illustrate the impact on subsequent data analysis, the influence on two vegetation indices is briefly analysed. Results show that the radiometric and spectral stability both have a high impact on the uncertainty of the narrow-band Photochemical Reflectance Index (PRI), and also the broad-band Normalized Difference Vegetation Index (NDVI) is affected.

1. Introduction

With the advent of new satellite sensors such as the ESA Sentinels, there is a growing demand for highly reliable and well-documented Earth observation data to fulfil the data needs for COPERNICUS services. To underpin the importance of this topic, the Committee on Earth Observation Satellites (CEOS) initiated the Quality Assurance Framework for Earth Observation (QA4EO), which demands that all "Data and derived products shall have associated with them a fully traceable indicator of their quality" [1]. In addition to the requirements of traceability of measurements, and the concept of data Quality Indicators (QIs), a concept of uncertainty of measurements is included in the QA4EO guidelines. The guidelines [2] are themselves a link to the Guide to the expression of Uncertainty in Measurements (GUM) issued by the Joint Committee for Guides in Metrology [3]. In the field of airborne hyperspectral remote sensing, the FP7 project EUropean Facility for Airborne Research (EUFAR) developed a set of harmonized QIs for Level 1 (calibrated at-sensor radiance) and Level 2 (orthorectified ground reflectance) data [4], which also included the development of a full error propagation concept [5]. Extending the EUFAR developments, an exhaustive uncertainty analysis was carried out for the Airborne Prism Experiment (APEX) sensor [6,7], and, on a smaller scale, for parts of the DLR hyperspectral pre-processing chain [8].

For the design of the upcoming spaceborne EnMAP mission, the CEOS QA4EO guidelines will be followed. In order to do so, a set of quality indicators is derived within the operational processing chain of the ground segment. For each dataset, radiometric properties (e.g., striping or saturation artefacts) as well as environmental conditions (e.g., percentage of cloud and haze) will be documented in a quality layer and within the metadata. In order to guarantee an independent validation, additional in-flight validation activities will be carried out under the lead of the Deutsches GeoForschungsZentrum (GFZ), and compared to international CalVal activities. An additional preparation activity of the EnMAP mission is the early availability of simulated datasets generated by the EnMAP End-to-End Simulation tool (EeteS, [9]). Having this tool available, studies on the expected uncertainty related to EnMAP data can be conducted. As the instrument is yet to be completed and launched, requirements on an instrument level (e.g., the ground sampling distance or the spectral bandwidth) and requirements related to the laboratory calibration as well as requirements for the in-orbit operation (e.g., [10]) can be used for the uncertainty estimation.

Within this study, the influence of these calibration requirements on the Level 2A product, *i.e.*, the uncertainty related to the bottom-of-atmosphere (BOA) reflectance data is investigated. In order to do so, a Monte-Carlo approach for uncertainty estimation developed within the FP7 EUFAR HyQuaPro project [5] is extended and applied to a simulated EnMAP Level 1B TOA-Radiance dataset for Barrax, Spain. The uncertainty analysis is conducted separately for two independent input parameters: (a) radiometric stability and (b) spectral stability. After the estimation of the probability distribution functions (PDFs) for these parameters, a larger number of realisations (150 in case (a), and 41 in case

(b)) are generated. Next, the ATCOR atmospheric correction [11] is carried out for the test scene, using each of these realisations as input, thereby including the radiometric and spectral calibration uncertainty of the Level 1B TOA-Radiance product while treating ATCOR as a "black box". The resulting ground reflectance images—each being a realisation of the underlying PDFs of the uncertain inputs—are then analysed in order to estimate the resulting uncertainty in ground reflectance. In a strict sense, the resulting product is a hemispherical-directional reflectance factor product. However, for simplicity, the shorter term reflectance will be used. In addition, the auxiliary products of the atmospheric correction are analysed, and the related uncertainty in the retrieved atmospheric parameters (water vapour and aerosol optical thickness) and the auxiliary product dense dark vegetation (DDV) maps is addressed. Finally, in order to demonstrate the impact on thematic products, well-known vegetation indices (the narrow-band Photochemical Reflectance Index (PRI) and the broad-band Normalized Difference Vegetation Index (NDVI) are calculated using the generated realisations, and analysed regarding the resulting uncertainties.

Following this approach, the impact of the radiometric and spectral system calibration requirements can be linked to the resulting uncertainties in the Level 2A product expressed in ground reflectance, and can be also linked to resulting uncertainties in thematic products.

2. Method and Materials

2.1. EnMAP System Requirements

The EnMAP instrument is spaceborne imaging spectrometer covering the wavelength range between 420 and 2450 nm with a spectral sampling distance of 5.5–11.5 nm (as full-widths half maximum (FWHM)). The EnMAP instrument design is a prism-based dual-spectrometer, with a visible and near infrared (VNIR) spectrometer covering the spectral range between 420 and 1000 nm, and a short-wave infrared (SWIR) spectrometer covering the range between 900 and 2450 nm. The expected signal-to-noise ratio is better than 400:1 in the visible and near-infrared, and 180:1 in the short-wave infrared. When pointing at nadir, the ground sampling distance is 30 m resulting in a swath width of 30 km. For a detailed description of the mission, the instrument and the ground segment, the reader is referred to e.g., [12,13] and the publications within this special issue (e.g., [14]).

In the context of this study, the key instrument requirements are the radiometric stability and the spectral stability. For EnMAP, the requirement for the absolute radiometric calibration accuracy is better than 5%, having a radiometric stability of ±2.5% (standard deviation) between two consecutive calibrations. The targeted spectral calibration accuracy is 0.5 nm for the VNIR and 1 nm for the SWIR, and a spectral stability of better than 0.5 nm [10]. Note that the spectral smile requirement (*i.e.*, the change in centre wavelength of a band as a function of the spatial cross-track position) is below 20% of a spectral pixel. Additional sources of uncertainty include stray light and polarization sensitivity, the latter is expected to be smaller than 5% for EnMAP. These additional factors are not addressed in this paper. When compared to similar spaceborne imaging spectrometers such as HYPERION, the requirements posed on the instrument in-orbit performance are challenging: Hyperion was found showing spectral shifts of 1–1.5 nm in the VNIR and 2.5–3 nm in the SWIR, and an absolute radiometric difference to airborne and in-situ measurements of ~10% in the VNIR and ~20% in the SWIR [15].

In a similar way, the EnMAP requirements are checked against the typical accuracies achieved for airborne instruments. As DLR operated the HyMap whiskbroom scanner for over a decade [16,17], the experience from vicarious calibration and validation experiments showed that the radiometric stability over multiple surveys is well within 5%, which is the same margin as the EnMAP requirement. However, for the spectral calibration, spectral shifts of up ±2 nm for each of the four HyMap detectors were frequently observed using the methodology by [18]. It is worth noting that these shifts were highly stable over time, and must be seen relative to the HyMap spectral sampling interval of 15–20 nm (FWHM). Within the context of this study, an additional set of simulations were run using this decreased spectral fidelity scenario of ±2 nm shifts, which is a magnitude larger than the EnMAP requirement of better than 0.5 nm.

2.2. EnMAP Atmospheric Correction over Land

The ATCOR model is a software package for atmospheric and topographic correction of multispectral and hyperspectral imagery [19]. It uses a pre-compiled database of radiative transfer calculations based on MODTRAN [20] and HITRAN 2013 data. The main features of ATCOR are: a pre-classification of the scene (land, water, haze, cloud), retrieval of atmospheric parameters (aerosol optical thickness, water vapour), and the surface reflectance retrieval accounting for the adjacency effect. For the compensation of topographic effects a digital elevation model is needed [11,21]. As stated before, within this paper the term "reflectance" is used for brevity, and relates to the "hemispherical-directional reflectance factor".

The algorithms used for the aerosol type and aerosol optical thickness (AOT) retrieval are based on a modification of the approach by [22]. This approach is based on the existence of reference pixels with known reflectance behaviour, namely pixels containing dense dark vegetation (DDV), and the assumption that for these pixels the reflectance values in the SWIR are correlated to the reflectance values in the red and blue parts of the spectrum. Therefore the accuracy of the AOT retrieval depends on the availability and the correct identification of DDV pixels, and the validity of the assumption on the spectral correlation between SWIR and VNIR for these pixels. For scene-based water vapour retrieval, the atmospheric pre-corrected differential absorption technique (APDA) is used (see [23]). The considerations when applied to spaceborne imaging spectrometer data are discussed in detail in [24].

Within ATCOR, additional options are the removal of thin cirrus clouds and haze [25]. Hyperspectral pushbroom imagery affected by spectral smile (e.g., EnMAP) can be corrected. Then, the spectral smile shift across the detector array is parametrized with a fourth-order polynomial function for each channel, based on the instrument optical design model or measured laboratory data [26]. Other features are the spectral calibration using atmospheric absorption features and the radiometric calibration using *in-situ* ground reflectance measurements.

2.3. The EnMAP Simulator and Test Scene Generation

As part of the system's development, the EnMAP End-to-End Simulation tool was developed at the GFZ to provide an accurate simulation of the entire image generation, calibration and processing chain. EeteS has been used to assist with the overall system design, the optimization of fundamental

instrument parameters, and to understand the effects of instrumental and environmental parameters on the resulting image characteristics and to investigate the limitations for parameter retrieval [9,27,28].

An artificial hyperspectral image was used as input to EeteS to generate EnMAP like radiance images for the study area in Barrax, Spain. This well-known study area consists of dry lands and irrigated farmland, and was used in a large number of hyperspectral CalVal activities such as the ESA SPARC-2004, Sen2Flex and DAISEX campaigns [29].

The image was generated based on a real Landsat 7 ETM+ image that was transformed calculating the inversion of a coupled soil-leaf-canopy and atmosphere radiative transfer modelling (SLC, [30]). The image has a final size of 1000 × 1000 pixels, 1021 bands in the wavelength range between 420 and 2460 nm and a pixels size of already 30 m meaning that no spatial simulation was performed within EeteS. As a consequence, the imagery used in this study and all generated data products are in raw sensor geometry and are not geo-referenced. In the first step of the EeteS simulation, the data was transformed into raw EnMAP DN data using a series of forward processing steps that model atmospheric conditions and account for spectral and radiometric differences between the two detectors. The software then simulates the Level 1B processing including the onboard calibration. The resulting at-sensor radiance image has a total of 242 bands, and having the typical EnMAP signal-to-noise and processing properties. It is worth noting that 20 bands are located within the overlap of the first and second spectrometer, and that none of these partially overlapping bands were removed in the subsequent processing.

2.4. Overview of the Uncertainty Estimation—The EUFAR Approach

2.4.1. General Concept

According to the GUM approach for estimating the standard uncertainty [3], the measurand y is determined from N other quantities, and the functional relationship f:

$$y = f(x_1, x_2, \dots, x_N) \qquad (1)$$

In case of this study, the ground reflectance is considered as the measurand, while parameters such as the radiometric sensor calibration, the spectral sensor calibration, the knowledge on aerosol type and aerosol optical thickness *etc.* are quantities having a functional relationship with ground reflectance. Note that also the inputs can be considered as measurands which also depend on other input factors, and that these input quantities x_1, x_2, …, x_N also have uncertainties linked to them.

When estimating the combined standard uncertainty $uc(y)$, which is the standard deviation of the measurement result *y*, the associated standard deviations of each input parameter x_i have to be addressed. These input parameters and their standard uncertainty $u(x_i)$ can be derived from the probability distribution function (PDF) which represents the possible values of the input quantity x_i. This PDF can derived by repeated measurements (denoted as "Type A evaluation"), or by existing assumptions or knowledge of the distribution ("Type B evaluation").

2.4.2. Adaptation to Hyperspectral Data

Within the EUFAR JRA2, a concept on how to address the uncertainty in airborne hyperspectral data products was developed and applied to airborne test datasets [5]. As analytical models have their limitations whenever the underlying model is highly complex, the decision was made to use a Monte-Carlo approach. In case of the atmospheric correction, the complexity of the model, the number and the value range of input parameters, and also the non-linearity of processes, can best be tracked by a Monte-Carlo approach. Therefore, the EUFAR concept of the Monte-Carlo uncertainty analysis for hyperspectral imagery consists of the following steps:

(1). Define the inputs and outputs of the model (*i.e.*, make an assumption on the functional relationship function f within the GUM approach)

(2). Decide which inputs are treated as uncertain (*i.e.*, define the input parameters x_i)

(3). Derive the probability distribution of the uncertain inputs (*i.e.*, get $u(x_i)$ using either a "Type A" or a "Type B" evaluation)

(4). Generate many possible realities of the uncertain inputs by repeated sampling from their probability distributions (*i.e.*, generate a large number of realisations of x_i)

(5). Run the model for the simulated realities and store the results (*i.e.*, generate a large number of simulated measurement results y)

(6). Analyse the model results (*i.e.*, derive $u_c(y)$ as the standard deviation of the measurement result y)

2.4.3. Implementation for the Simulated EnMAP Data

In the context of this study, this scheme is concretised by the following steps:

(1). Define the inputs and outputs of the model

As the influence of the instrument calibration stability is investigated, the calibrated at-sensor radiance data (Level 1B) is used an input. For this purpose, the simulated EnMAP scene of Barrax, Spain is used. The output is then the data product which most end users are expected to use, *i.e.*, the atmospherically corrected ground reflectance product (Level 2A). As the ATCOR approach is scene-based, no additional auxiliary inputs are required.

(2). Decide which inputs are treated as uncertain

Within this study, two parameters are investigated—the mentioned radiometric stability between two consecutive calibrations in test case (a), and the spectral calibration accuracy in case (b). Based on experience with airborne imaging spectrometers, the radiometric offset is usually treated adequately by the measurement of the internal dark current and the subsequent subtraction. In case of EnMAP, the dark signal measurement will be conducted before and after each image acquisition enabling even the correction of a linear variability. In contrast, the signal amplification (*i.e.*, radiometric gain) is more critical. Consequently, only the radiometric gain factors are included within this uncertainty estimation.

It is important to note that radiometric test case (a) and the spectral test case (b) are treated separately. As the spectral and the radiometric stability have an influence on the ground reflectance, one could argue that a combined analysis is required. However, as the aim of this experiment is the

estimation of the uncertainty in ground reflectance related to each of these parameters, and not the total uncertainty budget, an additional separate set of experiments would be required.

(3). Derive the probability distribution of the uncertain inputs

As the EnMAP instrument is yet to be launched, the PDF of these input parameters cannot be derived from repeated measurements. Therefore, a "Type B" evaluation of standard uncertainty is used [3] which is based on the manufacturer's specification documented in the system requirements. For case (a), the system requirement for radiometric stability of ±2.5% (assuming Gaussian distribution) is used. For case (b), the system requirement of the spectral calibration stability of 0.5 nm, and also the mentioned PDF derived from actual airborne hyperspectral data of ±2 nm are used.

(4). Generate many possible realities of the uncertain inputs by repeated sampling from their probability distributions

One possible way to generate these realities would be to simulate Level 1B data cubes representing these properties. However, in the case of ATCOR, a straightforward way is possible to achieve this. In general, the relationship between the at-sensor radiance L, the raw DN and atmospheric properties can be simplified as:

$$L = L_{path} + L_{reflected} = L_p + \frac{\tau \rho E_g}{\pi} = c0 + c1 DN \tag{2}$$

where L_p, τ, ρ and E_g are the path radiance, ground-to-sensor atmospheric transmittance, surface reflectance, and global flux on the ground, respectively, and the terms $c0$ and $c1$ represent the radiometric offset and gain [19].

For case (a), a sensor calibration file can be passed to ATCOR where the bandwise gain and offset coefficients are given. In case of calibrated Level 1B input data and an instrument with a valid calibration, the gain factors c1 are set to one and the offsets $c0$ are zero for each band. In case of an applied in-flight calibration, these gain and offset values are adjusted representing the improved instrument calibration. Within this study, the gain factors are now altered in order to simulate the radiometric stability of the instrument. This is done by adding random numbers to the gain factors. The random number generator used in this study is the IDL routine RANDOMN, which is based on the Box-Muller method [31] for generating normally-distributed random numbers in double precision, which are then scaled to match the assumed standard variation of ±2.5%. Next, the number of required realisations can be investigated during this step, as the total bandwise distribution of the gains should match the input PDF. In this case, a total of 150 realisations were necessary so that these calibration files match the expected distribution.

For case (b), the spectral stability, this step is conducted in a different way. As the spectral shifts cannot occur independently for each channel of a detector array, all bands of the corresponding detector were shifted equally. As a result, the shifting of the band centre wavelength for each of the two detector arrays by 0.1 nm is resulting in a total of 41 realisations for the 2 nm shift scenario, and 11 realisations for the 0.5 nm shift scenario. Within the ATCOR approach, the monochromatic atmospheric LUTs are then resampled to match each of these 41 realisations. The scenario of 0.5 nm shift is then conducted by selecting the 11 corresponding realisations.

(5). Run the model for the simulated realities and store the results

Within this step, the ATCOR atmospheric correction is carried out for each of the realisations. For this purpose the ATCOR version tailored to EnMAP is used, which includes the EnMAP acquisition configuration (*i.e.*, channel filter functions, radiometric and spectral calibration files). It will be the same version as implemented in the Processing Chain of the EnMAP ground segment. The set-up of ATCOR is identical in all cases, and is listed in Table 1. For test case (a), this step is resulting in a total of 150 atmospherically corrected scenes. In case (b), the outputs are 41 scenes.

Table 1. Set-up of ATCOR parameters used in this study. (*): note that the finally used bands can be different in case of the spectral shift scenario.

Parameter	Value	Parameter	Value	Parameter	Value
Variable AOT	Yes	Aerosol type	rural	WV measurement channel	1.1318 μm (*)
Variable WV	Yes	Adjacency effect range	1 km	WV reference channels	1.0740 μm (*) & 1.2148 μm (*)
Haze removal	No	Interpolation of 760 O2 bands	no	Dark reference pixel SWIR band	2.1327 μm (*)
Shadow removal	No	Interpolation of WV bands (725/825/940/1130/1400/1900)	no	VIS calculation reference bands	0.44472 μm (*) & 0.65820 μm (*)
Terrain correction	No	WV map smoothing	100 m × 100 m	Removal of overlapping bands between VNIR & SWIR	no
BRDF correction	No	WV model	With band regression	-	-

(6). Analyse the model results

In case of this uncertainty study, the model output y are ground reflectances as generated by ATCOR, and the standard deviation in ground reflectance over all realisations $uc(y)$ can be considered the combined standard uncertainty. As the atmosphere has a wavelength-dependent effect on the signal sensed, the combined standard uncertainty has to be addressed as wavelength-dependent. Thus, for the radiometric test case (a), the analysis can be conducted in a simple and straightforward way by calculating the bandwise standard deviation over all realisations for each band.

For test case (b) which was using a shifting scenario, an additional weighting step is required. As smaller spectral shifts are more likely to occur than larger shifts, the model results with smaller shifts are given a higher weighting in the analysis step assuming a Gaussian distribution. For the 0.5 nm shifting scenario, the nominal shift and the ±0.1 nm shifts are represented with a weighting factor of 3, the ±0.2 and ±0.3 nm shifts with a weighting factor of 2, and the ±0.4 and ±0.5 nm shifts with a single weighting. Also, the 2 nm shifting scenario is handled accordingly.

For a better presentation of the uncertainty values, four regions of interest (ROIs) distributed over the scenes are selected (Figure 1). These ROIs represent three different classes of vital vegetation (dark, intermediate and bright, the name related to the relative reflectance of each class in the NIR) and a class of mixture between soil and non-photosynthetic active vegetation, representing different spectral surface properties (Figure 2). Also, the statistical description of the full scene is given whenever meaningful.
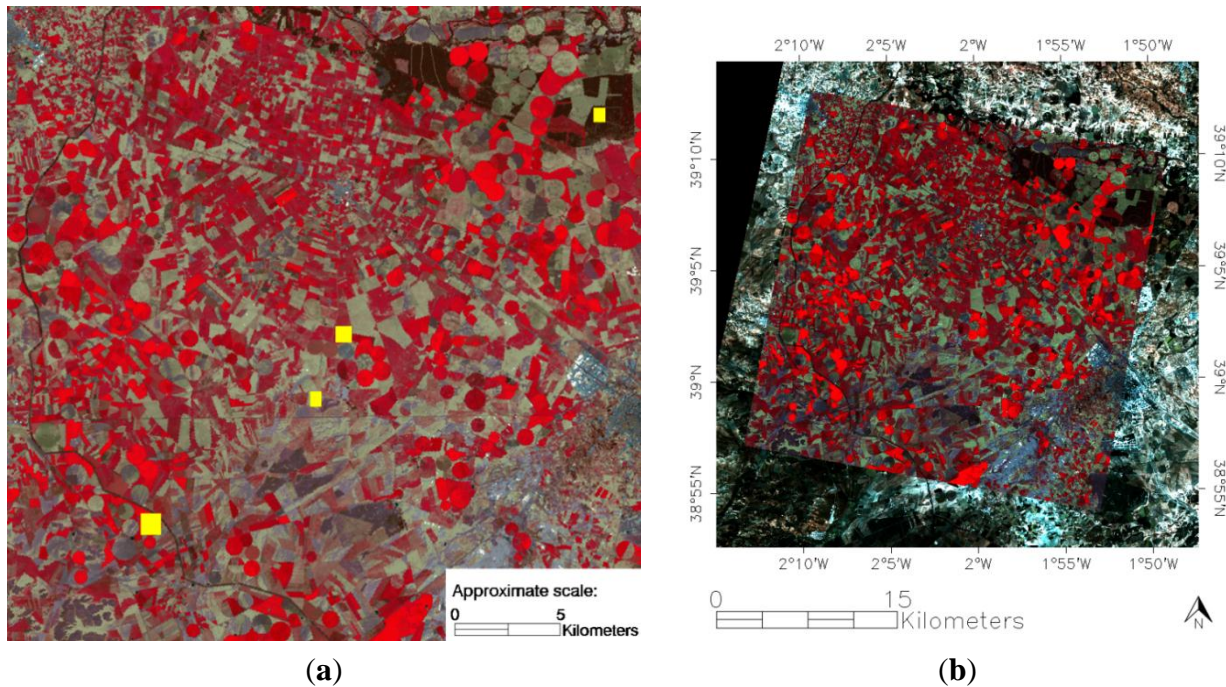
(**a**) (**b**)

Figure 1. Overview of the simulated EnMAP scene "Barrax"; (**a**, left) colour infrared composite in original sensor geometry (channels at 895, 652, 548 nm used for R-G-B, linear image stretch); the regions of interest used in this study are represented by yellow boxes of the approximate size; (**b**, right) for illustration: overlay of the same image as in (**a**) on an ortho-rectified Landsat 8 scene displayed as true colour composite (Landsat 8 channels 3-2-1 used for R-G-B, linear image stretch).
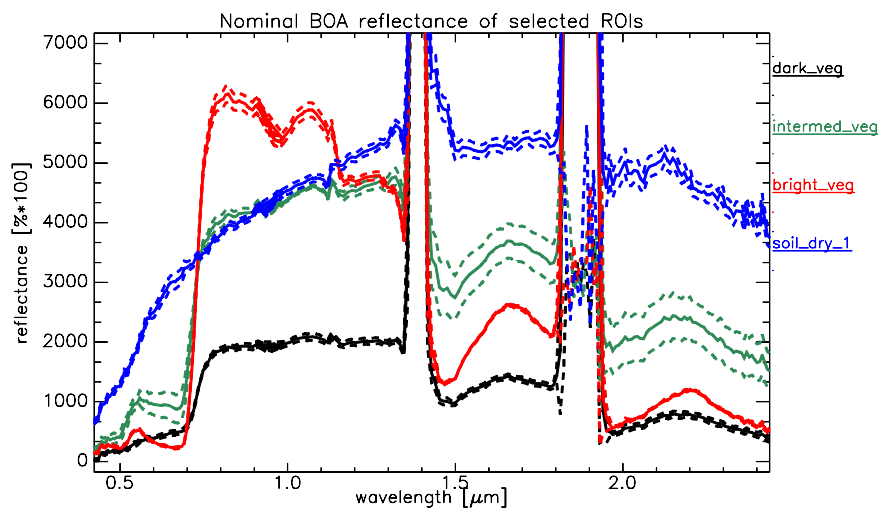
Figure 2. Bottom-of-atmosphere (BOA) reflectance spectra of the four used ROI classes (solid lines) and the related standard deviation (dotted lines). For the vegetation classes, the name prefix "dark", "intermediate" and "bright" relates to the relative reflectance in the NIR.

2.5. Further Influence on Thematic Products

In order to give an illustrative example on how the uncertainty included in the Level 2A product can affect the generation of further thematic products, two widely used vegetation indices were calculated

on all generated realisations. In the subsequent analysis, the standard deviation of the index values serves as an approximation of the related uncertainty of the thematic products.

As a first example, the Photochemical Reflectance Index (PRI) is used, which is usually calculated as the following normalized band ratio:

$$PRI = \frac{R531 - R570}{R531 + R570} \tag{3}$$

with R531 and R570 being the ground reflectance values of the bands with the centre wavelength closest to 531 and 570 nm (e.g., [32]).

The PRI is chosen as it is based on subtle absorption features of bio-chemicals (xanthophyll, carotenoids and chlorophylls), and is related to photosynthetic efficiency, light use efficiency as well as water stress [32,33]. The PRI is frequently used on leaf, canopy and ecosystem level, but the meaningfulness when applied at satellite scale is critically discussed [32], and high-spectral resolution instruments such as EnMAP have the potential to overcome some of the problems. Also, the PRI was found to be sensitive to atmospheric scattering [34], therefore being a good example in context of this study.

For comparison, the broad-band Normalized Difference Vegetation Index (NDVI) is also calculated. The NDVI is using larger wavelength regions in the red (RED) and the near-infrared (NIR), and can be related to various vegetation parameters including leaf area index, biomass and chlorophyll content. The well-known equation is:

$$NDVI = \frac{NIR - RED}{NIR + RED} \tag{4}$$

In this study, EnMAP bands approximating the spectral response of bands 3 (RED) and 4 (NIR) of Landsat 7 ETM+ are used for the NDVI calculation.

3. Results and Discussions

3.1. Uncertainty in Ground Reflectance, Radiometric Case

When depicting single pixel spectral from the same image location from various realisations, the uncertainty in radiometric gain is represented in the form of uncorrelated bandwise variations similar to sensor noise (Figure 3a).

As set within the ATCOR processing parameters (see Table 1), all wavelength regions where atmospheric absorption occurs were not interpolated. Consequently, all wavelength regions with strong atmospheric influence, especially the water vapour absorption bands around 1400 and 1900 nm, are dominated by noise and do not contain a meaningful signal. However, when zooming in on a wavelength range affected by a weaker atmospheric absorption, *i.e.*, the WV reference feature at 1130 nm, no large impact is observed demonstrating that the atmospheric correction is adequate (Figure 3b).
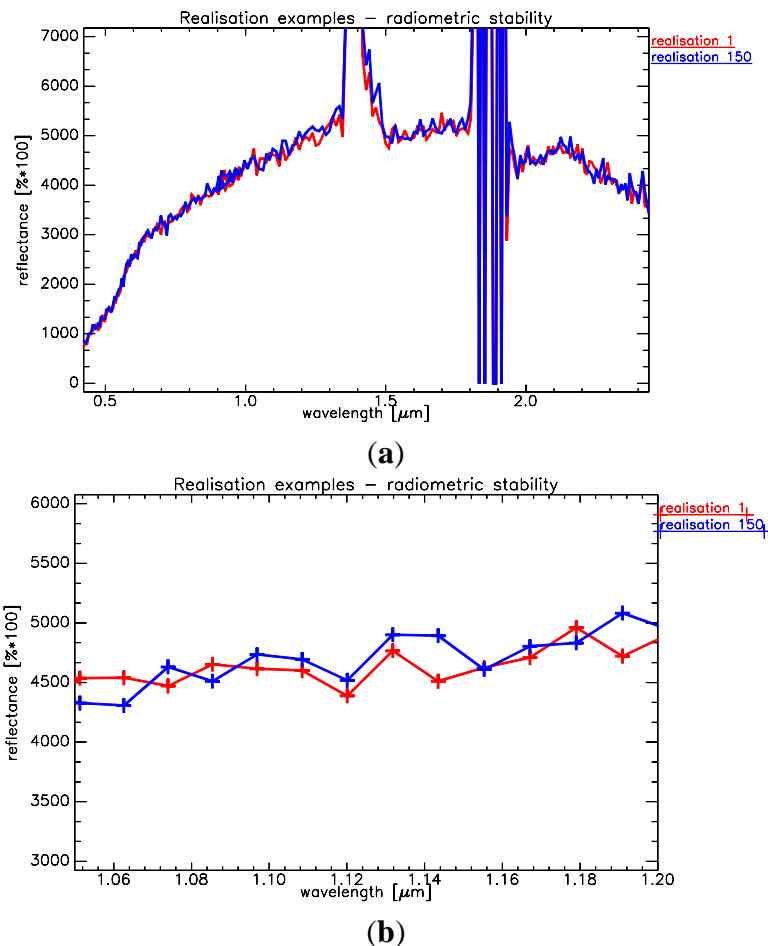
(a)

(b)

Figure 3. Plot of the reflectance spectra of two realizations of an image pixel; (**a**) full range; (**b**) zoom on the minor water vapour absorption feature at 1130 nm.

When analysing the absolute spread across all 150 realisations for a test ROI (Figure 4), the wavelength dependence of the effect is clearly visible. It is already obvious that the variability is larger for parts of the spectrum having higher reflectance values. The reason for this is that the radiometric gain was altered in the various realisations, and thus this multiplicative effect increases with ground reflectance. The absolute magnitude of this variability, calculated as the spread between the maximum and minimum value of all realisations, can reach up to 10% reflectance (absolute) for one ROI class.
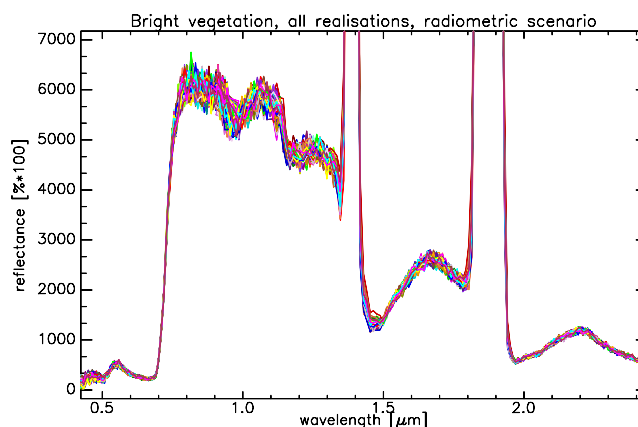
Figure 4. Plot of all realisations for the ROI "bright vegetation".

In order to illustrate this spread, the mean and standard deviation over all model results y are calculated, whereas the standard deviation is the combined standard uncertainty $uc(y)$. Again, the standard deviation increases with reflectance (Figure 5). Within the NIR plateau, the standard deviation for the given bright vegetation class can reach up to 1.5% reflectance absolute, and is less pronounced in other wavelength regions.
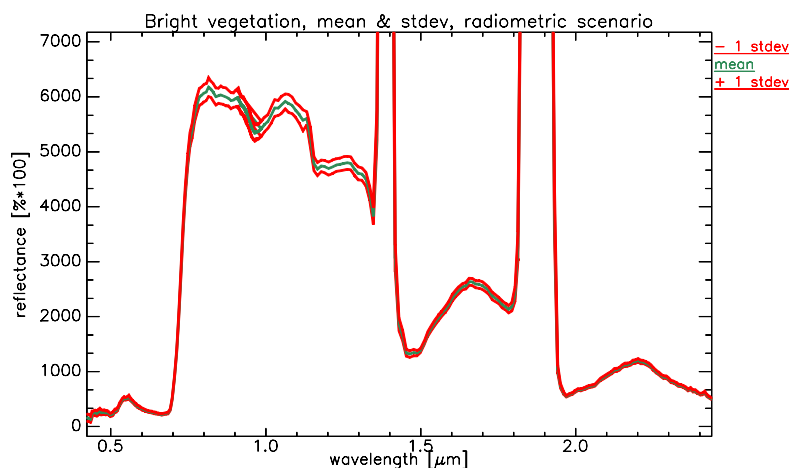

Figure 5. Plot of the mean spectrum and the standard deviation (stdev) calculated over all realisations for the ROI "bright vegetation".

When analysing the standard deviations and thus the standard uncertainty for all selected ROIs as well as for the whole image, the absolute value of $uc(y)$ is class- and wavelength dependent (Figure 6). As before, the dependency on the ground reflectance of each class is clearly visible. However, also an additional general trend can be observed. That is, the variability generally increases for wavelengths below ~700 nm. Outside of atmospheric absorptions, the absolute magnitude of this standard uncertainty is in the order of 0.2%−1% reflectance absolute in the VIS, 0.5%−2% in the NIR, and 0.25%−1.5% reflectance in the SWIR.
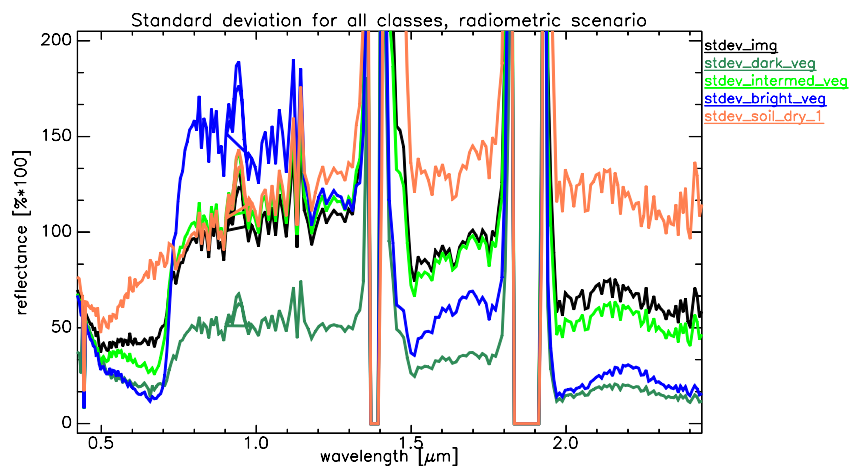

Figure 6. Plot of the absolute standard deviation (stdev) for all ROI classes, representing the combined standard uncertainty.

In order to exclude the influence of the different class reflectances, the relative variability is calculated as the ratio between the standard deviation across all realisations, and the mean of all realisations (Figure 7). In context of this study, this value is a good representation of the relative combined standard uncertainty $uc(y)$. One obvious result is that for all wavelengths above ~700 nm, the relative uncertainty is almost equal for all classes, having a magnitude of 2.5%. For wavelength shorter than 700 nm, a general exponential increase towards shorter wavelength can be observed, and the uncertainty is also depending on the LC/ROI class. This behaviour is related to the influence of aerosol scattering on the ground reflectance, and will be discussed in detail in Chapter 3.3.2. For the magnitude, as the aerosol scattering can be approximated as an additive effect on the sensed signal, surfaces having a lower reflectance in this wavelength range are more affected than brighter surfaces. For the given classes (see Figure 2), the soil and dry vegetation class which has the highest reflectance in this wavelength range, the influence is small, while the dark and bright vegetation classes both having a low reflectance in this wavelength range are heavily influenced resulting in a large uncertainty.
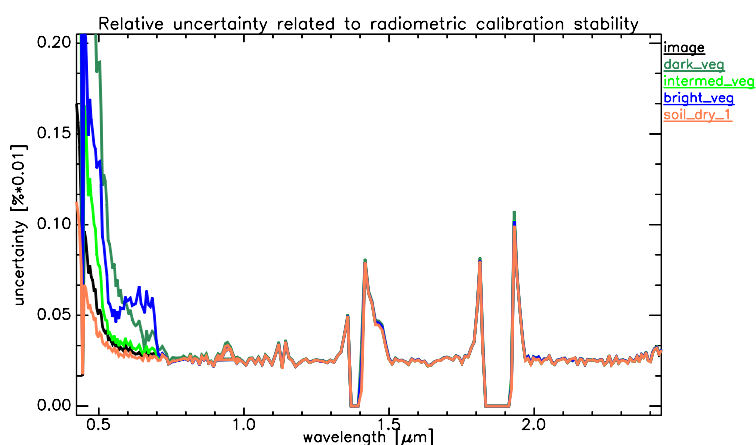

Figure 7. Plot of the relative standard deviation (stdev) for all ROI classes, representing the relative combined standard uncertainty.

To summarize, when assuming that the radiometric stability of EnMAP is 2.5% between two consecutive calibrations, the relative uncertainty in ground reflectance is about 2.5% (relative) for wavelengths above 700 nm. For wavelengths highly influenced by aerosols, the uncertainty is a function of the surface brightness and, in the extreme case of dark vegetation, can reach 50% or more for bands below 450 nm.

3.2. Uncertainty in Ground Reflectance, Spectral Case

The results for the spectral stability scenario are analysed in a similar way. When depicting in Figure 8 the spectrum of the same pixel as before in Figure 3, the influence of the spectral calibration uncertainty is different to the radiometric case.

First, the magnitude of the spectral shift has a directly increasing influence on the resulting ground reflectance (Figures 8 and 9). As the set-up of this experiment also includes a run where no shifts are added, this run can serve as a reference for a correctly calibrated instrument. For example, around the water vapour feature at 1130 nm, the absolute variation in reflectance units compared to the reference

can reach up to 4% reflectance for the 0.5 nm shifts, and up to 14% reflectance for the 2 nm shifts. For bands close to, but not within, strong WV absorption features, the variation is ~1% and 5% reflectance for the 0.5 nm and the 2 nm shift scenario.
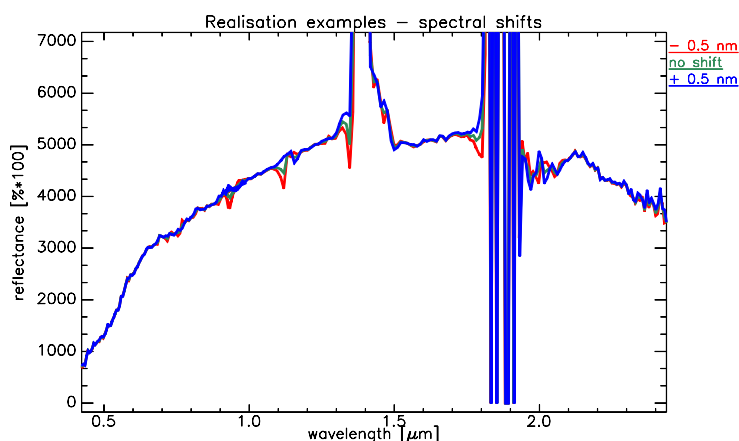

Figure 8. Plot of the reflectance spectra of three realizations of an image pixel, *i.e.*, having a shift of 0.5 nm towards shorter wavelengths (−0.5 nm), no shift, and a shift of 0.5 nm towards longer wavelengths (+0.5 nm).
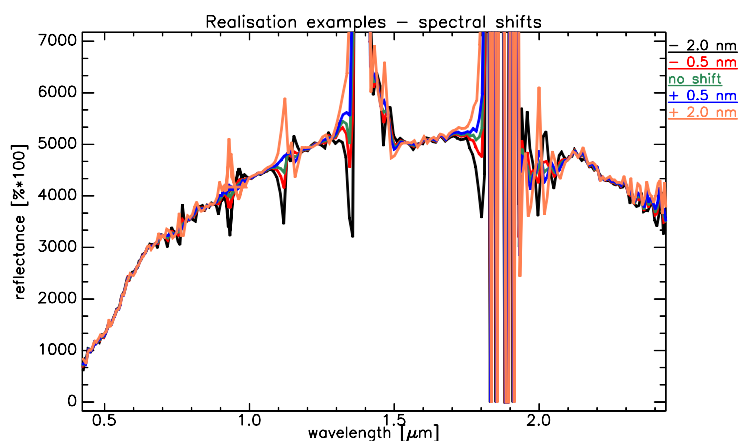

Figure 9. The same as Figure 8, now also including plots for the shifts by −2.0 nm and +2.0 nm.

Next, the differences in ground reflectance of the spectral shifts have only a significant influence in certain wavelength regions, whereas in the radiometric case all bands are affected. That is, all wavelength regions where atmospheric water vapour or oxygen absorption effects are corrected are affected (725, 760, 825, 940, 1130, 1400 and 1900 nm), while wavelength regions where the atmospheric influence is small have nearly identical reflectance values for the different shifts.

In addition, in wavelength regions where neighbouring bands show similar reflectance values, the shifting effect is low, while for wavelength areas with large band-to-band variations the influence on reflectances increases. This is illustrated in Figure 10, which shows the ground reflectance spectrum between 680 and 800 nm of a single vegetation pixel influenced by various spectral shifts. For wavelength regions with high band-to-band correlation (680–700 nm and 780–800 nm), the spectral shifts have little influences on the reflectance values. For the "Red Edge" (700–780 nm) having large band-to-band variations, the reflectance for a certain wavelengths can be altered by up to

~0.5% absolute in case of the 0.5 nm shifts, and by up to ~3% absolute in case of the 2 nm shift. In addition, as the inflection point of this wavelength area (*i.e.*, the wavelength position of the maximum increase) is frequently used as an indicator for plant stress, the subsequent thematic analysis is heavily influenced, as the wavelength shift caused by the spectral calibration uncertainty might be mistaken for a change in plant health. Also depicted in Figure 10 is the oxygen absorption(s) around 760 nm. Depending on the direction of the spectral shift (*i.e.*, a shift towards longer or towards larger wavelengths), an overcorrection for one band is followed by an undercorrection for another band, or vice versa. In case of no shift, the oxygen absorption is corrected adequately. This over- and undercorrection is also illustrated in Figure 11 for the water vapour absorption at around 1130 nm.
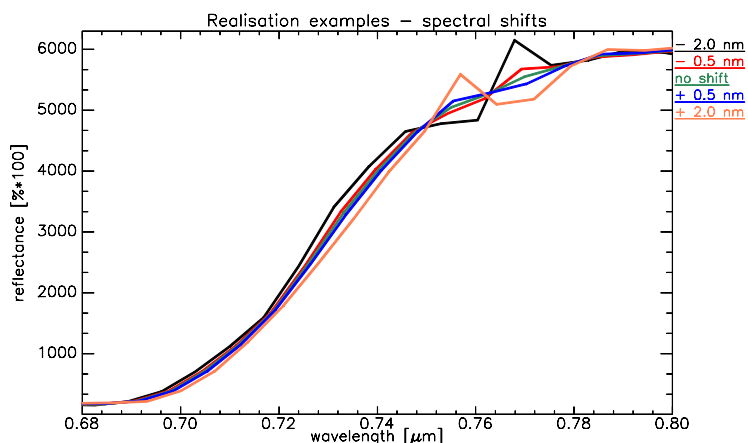

Figure 10. Plot of the reflectance spectra of five realizations, zoom on the red edge region of a ground pixel covered by vegetation.
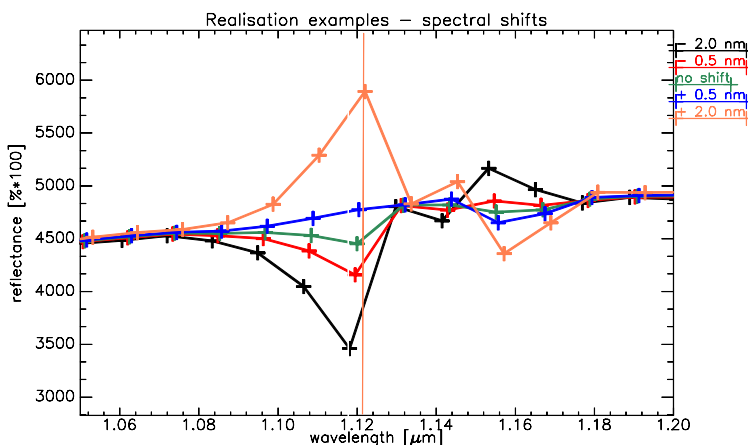

Figure 11. Plot of the reflectance spectra of five realizations, zoom on the minor water vapour absorption feature at 1130 nm. The vertical black and orange lines illustrate the magnitude of the shift of −2.0 nm up to +2.0 nm.

When investigating the full variability of model outcomes for one of the ROIs, the previously discussed differences to the radiometric scenario (a) can be observed. When comparing the realisations for the bright vegetation class (Figures 4 and 12, as well as Figures 5 and 13), the spectral shifts only affect wavelength regions which are affected by atmospheric absorptions, and the bands close to these wavelengths. In general, the magnitude of variation is smaller when compared to the radiometric case.
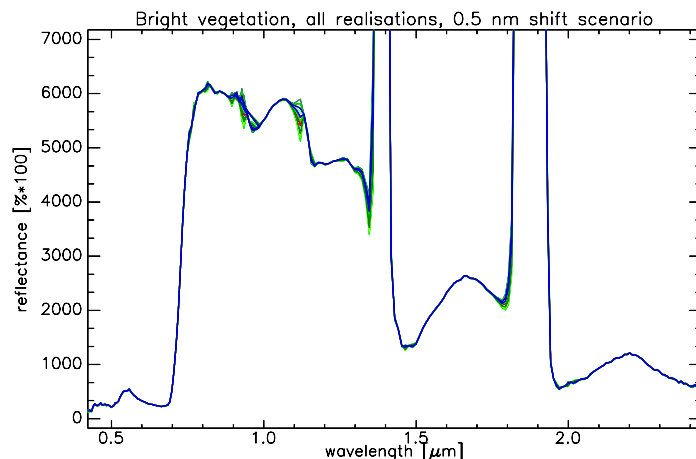
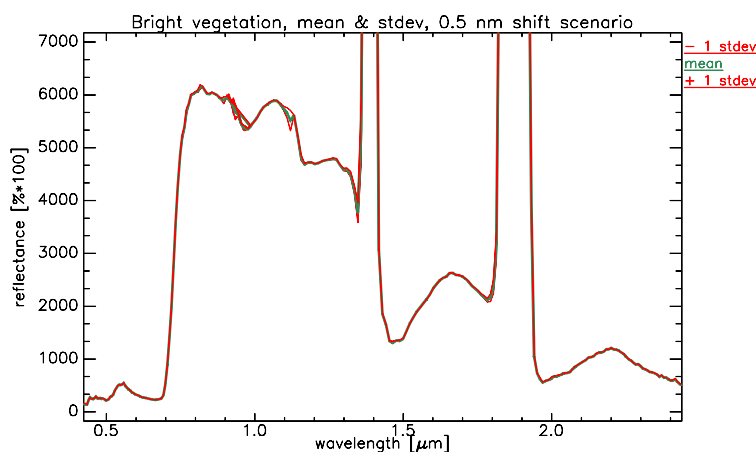**Figure 12.** Plot of all realisations for the ROI "bright vegetation".

Figure 13. Plot of the mean spectrum and the standard deviation (stdev) calculated over all realisations for the ROI "bright vegetation".

Also, the magnitude of the influence of spectral shifting depends on the land cover as represented by the different ROIs (see Figure 14), but the relative differences between the single classes are smaller compared to the radiometric scenario. The absolute magnitude of this combined standard uncertainty $uc(y)$ is below 1% reflectance absolute for wavelength outside atmospheric absorption regions, ~0.5%–2% reflectance absolute in the weaker water vapour absorptions and also in the CO_2 absorptions around 2.0 μm, and is also increasing up to 0.7% reflectance absolute toward the water vapour feature above 2.3 μm.

Regarding the relative combined standard uncertainty $uc(y)$, *i.e.*, the ratio between the standard deviation across all realisations, and the mean of all realisations, the influence of the different LUCs is negligible for all wavelengths above ~700 nm (see Figure 15). Next, for all wavelengths within the weaker atmospheric absorption features (*i.e.*, excluding the WV features around 1400 and 1900 nm), as well as bands close to these features, the relative uncertainties in ground reflectance are in the range of 2%–5% reflectance in case of the 0.5 nm shift scenario (Figure 15) and in the range of 4%–15% in case of the 2 nm shift scenario (Figure 16a). The overall spectral behaviour of the relative uncertainty is similar in both cases, with the 2 nm shift scenario having an increase in uncertainty by a factor of ~4–8 for most wavelength regions above 700 nm, and up to a factor of 50 for single bands in the VNIR range.

In comparison to the radiometric case (Figures 7 and 16a), the spectral shifting has a higher influence on single bands, while for the radiometric scenario, neighbouring bands are similarly influenced.
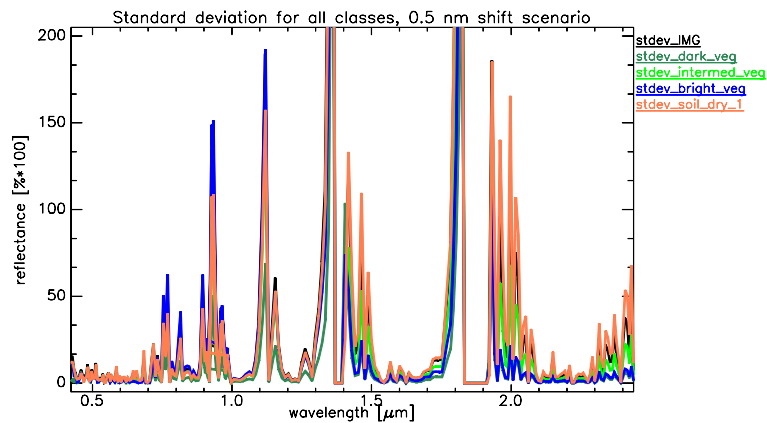

Figure 14. Plot of the absolute standard deviation (stdev) for all ROI classes, representing the combined standard uncertainty.
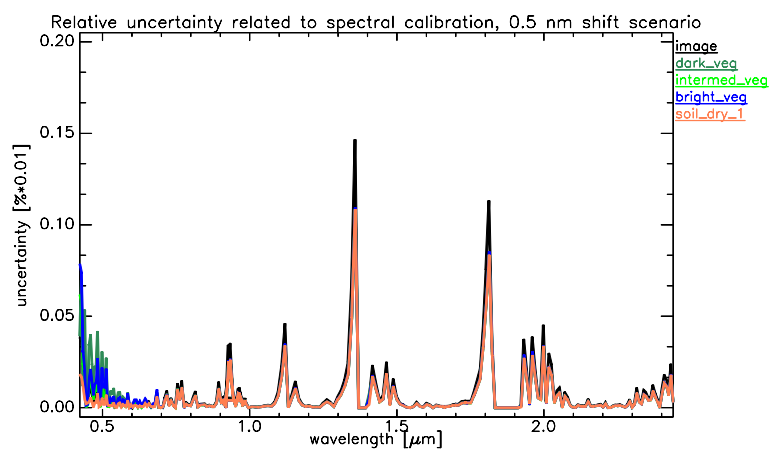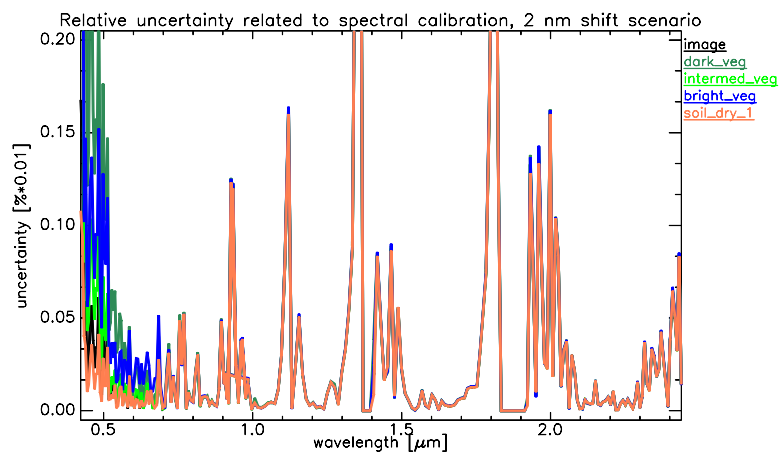

Figure 15. Plot of the relative standard deviation (stdev) for all ROI classes, representing the relative combined standard uncertainty of the 0.5 nm shift scenario.
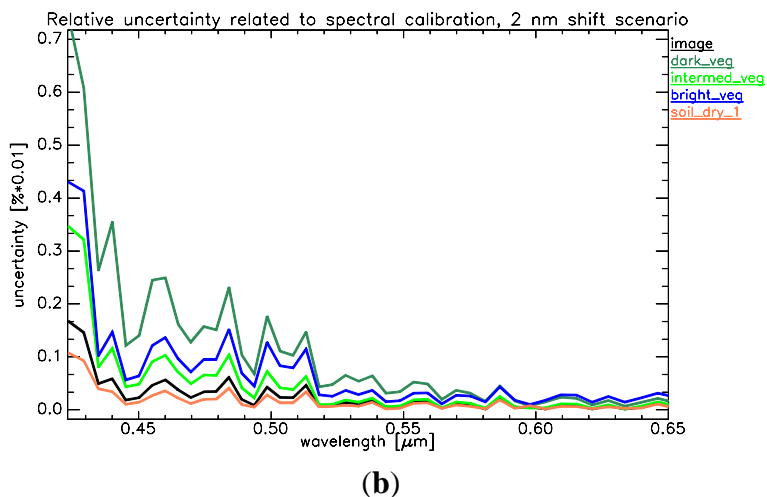

(a)

Figure 16. *Cont.*

(**b**)

Figure 16. Plot of the relative standard deviation (stdev) for all ROI classes, representing the relative combined standard uncertainty of the 2.0 nm shift scenario; (**a**) full spectral range; (**b**) zoom on the wavelengths below 650 nm.

When addressing the remaining surface-dependency of the combined standard uncertainty in ground reflectance, again the same general exponential increase towards shorter wavelengths as in the radiometric case is observed (Figures 7 and 16b). As before, the magnitude of the uncertainty is related to the overall reflectance in this wavelength range, with dark surfaces being more affected than bright ones.

3.3. Influence on Auxiliary Products

3.3.1. WV Retrieval

As the previous results suggest, there is a large influence of the radiometric and spectral calibration stability on the retrieval of atmospheric parameters immanent in the atmospheric correction. When analysing the water vapour retrievals (Table 2), the mean WV for the scene is comparable for all scenarios. In case of the radiometric scenario, the standard deviation and therefore the standard uncertainty is significant, having a magnitude of 2.7% relative, and an absolute value of 50.87 (g/cm^2 $\times 1000$). In case of the spectral scenario, the influence of spectral shifts in the magnitude of 0.5 nm has a related relative uncertainty of 0.8%, which increases up to 4.1% for the 2 nm shift scenario.

Table 2. Statistical description of the water vapour retrieval.

	WV Mean (g/cm^2 $\times 1000$)	WV Stdev, *i.e.*, Absolute Standard Uncertainty (g/cm^2 $\times 1000$)	WV Stdev % (Stdev/Mean) *i.e.*, Relative Standard Uncertainty	WV Max Spread (Max-Min)/Mean
Radiometric scenario	1911	50.87	2.7%	26%
Spectral scenario, 0.5 nm shifts	1904	16.63	0.8%	11%
Spectral scenario, 2 nm shifts	1911	78.50	4.1%	21%

When analysing the spatial patterns (Figure 17a–c), the uncertainty is not equally distributed over the scene, and does vary significantly as a function of the ground cover classes. While the spatial distribution pattern of the absolute uncertainty is similar for both spectral shift cases, the distribution pattern of the radiometric case is different.
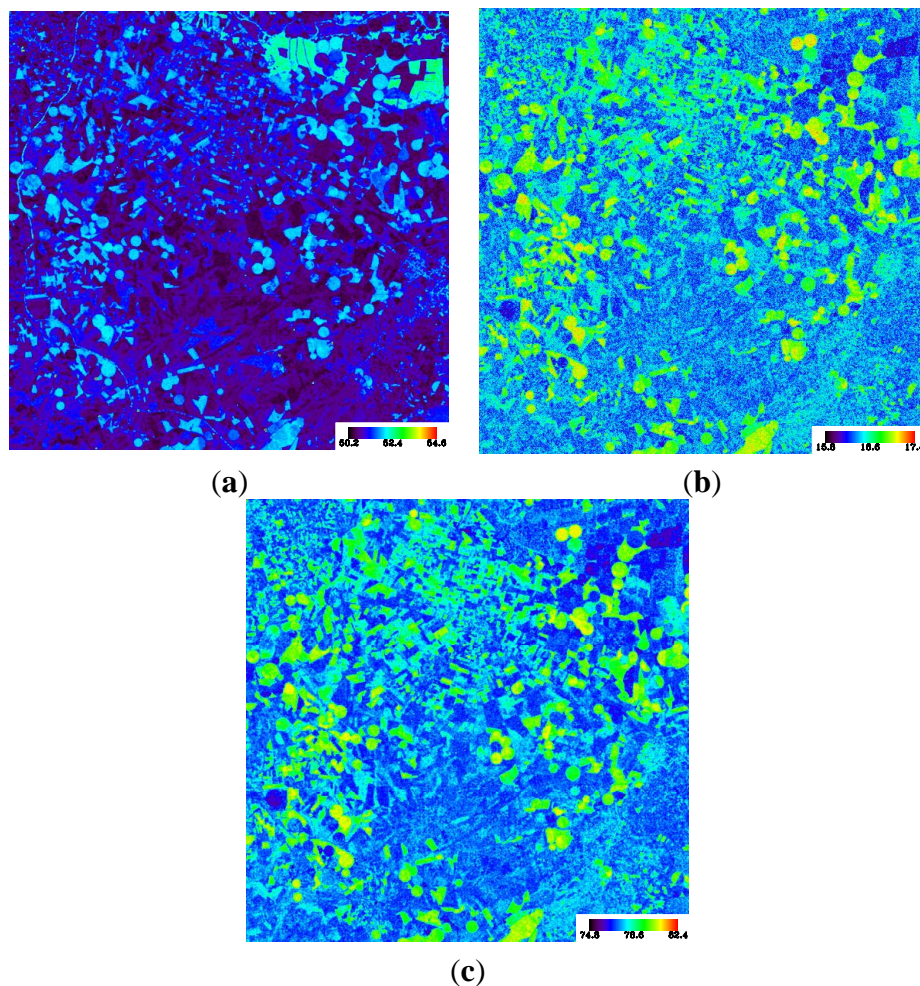

(**a**)

(**b**)

(**c**)

Figure 17. Standard deviation calculated over all WV maps; (**a**, top-left) radiometric scenario; (**b**, top-right) 0.5 nm shift scenario; (**c**, bottom-left) 2 nm shift scenario. Note that the data range and thus the colour coding is different for each image.

3.3.2. AOT Retrieval

For the retrieval of the aerosol optical thickness at 550 nm (AOT), the radiometric calibration stability has a significant influence on the AOT, as the relative standard uncertainty in AOT is 9.6% as an average value for the whole scene (Table 3). The influences of the spectral shifting scenarios are less pronounced, as the relative standard uncertainty related to the 2 nm shifts is 2.7% on average for the whole scene, and less than 1% for the 0.5 nm shift scenario. Regionally, this uncertainty can be much higher, as depicted in Figure 18. Even for the 0.5 nm shift (Figure 18b), a number of areas with an absolute relative uncertainty of 3 AOT units (~4% relative) occur, but for most areas of the image the uncertainty in retrieved AOT is close to 0. The difference is most notably in the border regions as the mean AOT values in the gap filled regions are different, as well as the AOT maps estimated from

the DDV because of a spatial smoothing. The AOT values are unitless; nevertheless, the values themselves are scaled by a factor of 1000 to fit into the integer data range. For the 2 nm shift scenario (Figure 18c), a general uncertainty of 2.3 AOT units (~2.5% relative uncertainty) can be observed for most areas, which increases up to 4.7 units (5.5% relative). In both cases, especially the borders of image regions having a similar AOT are affected (Figure 18b,c).

Table 3. Statistical description of the aerosol optical thickness retrieval.

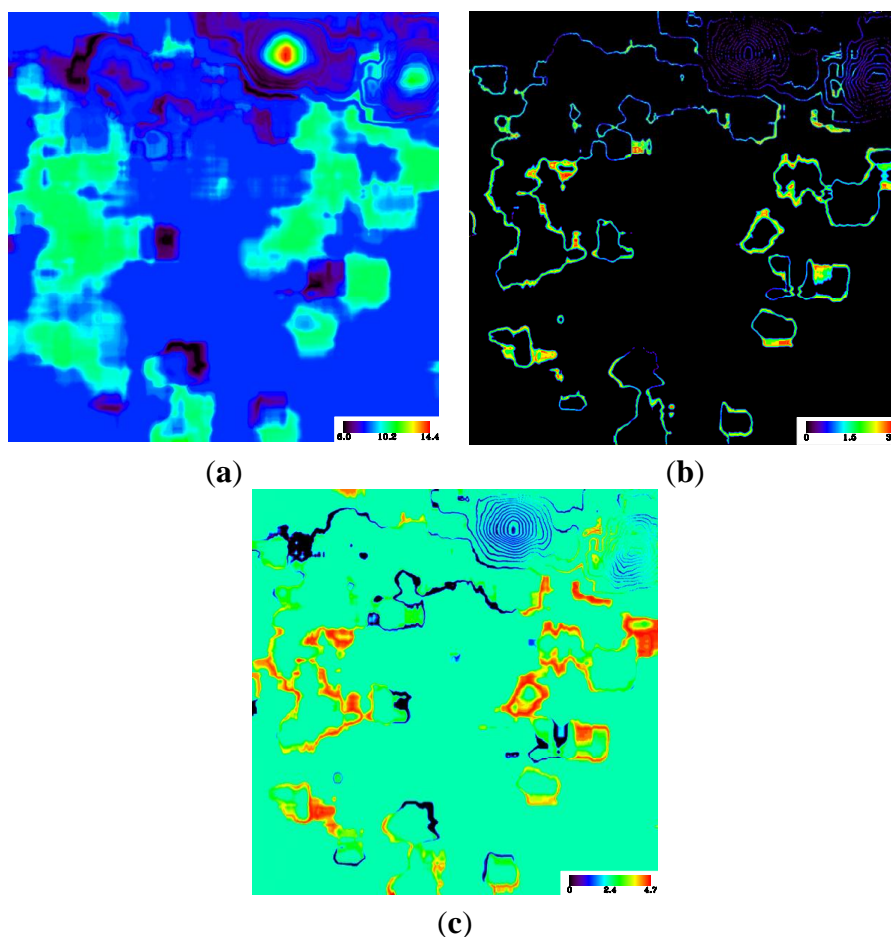|	AOT Mean (at 550 nm, Scaled by 1000)	AOT Stdev Absolute (at 550 nm, Scaled by 1000)	AOT Stdev % (Stdev/Mean)	AOT Max Spread (Max-Min)/Mean
Radiometric scenario	87.08	8.35	9.6%	152%
Spectral scenario, 0.5 nm shifts	84.50	0.09	<1%	92%
Spectral scenario, 2 nm shifts	85.42	2.27	2.7%	91%

(**a**) (**b**)

(**c**)

Figure 18. Standard deviation calculated over all AOT maps; (**a**, top-left) radiometric scenario; (**b**, top-right) 0.5 nm shift scenario; (**c**, bottom-left) 2 nm shift scenario. Note that the data range and thus the colour coding is different for each image.

For the radiometric case, the uncertainty related to most of the image areas is 8.2 AOT units, corresponding to a relative uncertainty of 9.4%, and up to 14.4 units absolute (~16% relative uncertainty). As before, the spatial variability is large (Figure 18a), but the differences between areas having a similar AOT and their borders is less pronounced.

3.3.3. DDV Maps

For a reference scene where no changes are made to the radiometric and spectral calibration, 9.4% of all pixels in the scene were classified as DDV. When shifting the spectral calibration by 2 nm, the percentage varies between 7.8% and 10.2%, and between 9.0% and 9.6% when shifting by 0.5 nm. For the radiometric case, the change in detected DDV pixels is larger, and varies between 4% and 15%.

When analysing the spatial distribution of DDV pixels over the image (Figure 19a,b), connected areas (*i.e.*, whole fields) are included or discarded in the DDV maps. This can be explained as the DDV pixel identification is based on thresholds, which are affected by the variability in the sensed signal and the underlying radiometric and spectral stability of the instrument. As a consequence, the AOT estimation for whole spatial areas can be associated with a higher uncertainty, while other areas show a relatively small uncertainty.
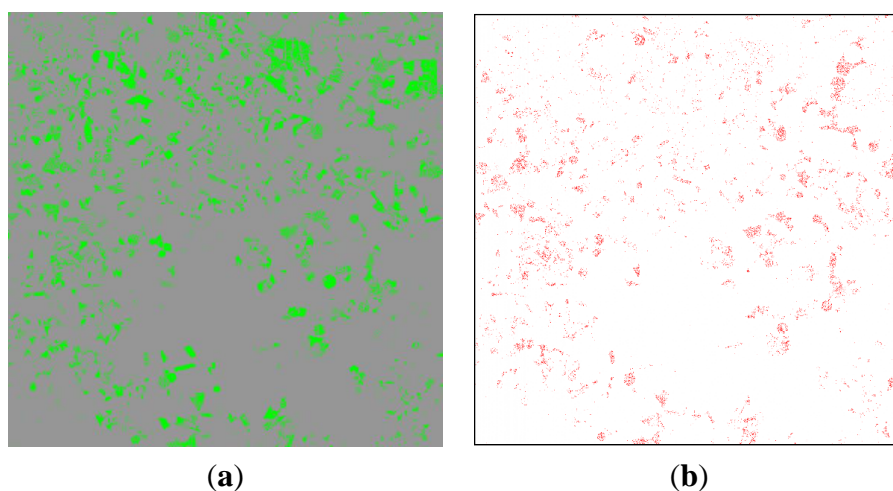

| (**a**) | (**b**) |

Figure 19. Spatial distribution of Dense Dark Vegetation (DDV) pixels; (**a**) distribution of the nominal scenario having no spectral shifts, where green dots represent DDV pixels; (**b**) difference image where red dots represent pixels classified as DDV pixels in the nominal case (**a**), but not classified as DDV in the +2.0 nm shift scenario.

3.4. Influence on Thematic Products—Example: Vegetation Products

Based on the generated ground reflectance images for all radiometric and spectral scenarios, the PRI and the broad-band NDVI were calculated. When analysing the results for the four ROIs (Tables 4 and 5), the following results can be observed. For all classes the mean values of each index are not altered, so no bias is introduced. In case of the broad-band index NDVI (Table 4), the influence of the spectral shift scenario is marginal. Only for a shift of ±2 nm, the variability and thus the uncertainty in the generated product is over 1%, but even then still not relevant. For the radiometric test case, the influence is more pronounced, and in the magnitude of 8%–9%.

Table 4. Relative uncertainty of the NDVI for selected ROIs.

	Dark_Veg Class, Relative Uncertainty in NDVI	Intermed_Veg Class, Relative Uncertainty in NDVI	Bright_Veg Class, Relative Uncertainty in NDVI	Soil_Dry_1 Class, Relative Uncertainty in NDVI
Radiometric scenario	8.2%	8.2%	8.2%	8.9%
Spectral scenario, 2 nm shifts	0.3%	0.1%	0.1%	1.3%
Spectral scenario, 0.5 nm shifts	<0.1%	<0.1%	<0.1%	<0.1%

Table 5. Relative uncertainty of the PRI for selected ROIs.

	Dark_Veg Class, Relative Uncertainty in PRI	Intermed_Veg Class, Relative Uncertainty in PRI	Bright_Veg Class, Relative Uncertainty in PRI	Soil_Dry_1 Class, Relative Uncertainty in PRI
Radiometric scenario	37.1%	62.9%	49.9%	17.4%
Spectral scenario, 2 nm shifts	12.1%	10.8%	7.9%	2.6%
Spectral scenario, 0.5 nm shifts	2.0%	2.0%	1.6%	<0.1%

When analysing the subtle narrow-band index PRI (Table 5), the picture is completely different. The radiometric scenario does affect the calculated index values by 17% for a dryland class up to 63% for the intermediate vegetation class. Also, for the spectral shifting scenario the resulting variability is non-negligible, ranging from ~3% for a dryland class to 12% for a dark vegetation class in case of the 2 nm shifts, and up to 60% in case of the 0.5 nm shifts. The underlying reason for this large uncertainty is that the PRI is based on a ratio of two bands at 531 and 570 nm, which are both highly affected by the AOT retrieval. As stated before, the uncertainty in ground reflectance increases exponentially towards shorter wavelengths, and can reach 15%–20% (relative) at 500 nm for certain land cover classes in the radiometric scenario. This large influence and the high class-dependency are critical for a meaningful interpretation of the results. Nevertheless, one must bear in mind that the PRI is a difficult test case, as the index relies on subtle changes in the spectrum, and the spectrally selective atmospheric scattering and its interaction within the vegetation canopies does have an influence of over 70% when using the PRI differences with view angle reported in [34].

4. Conclusions

Within this study, the influence of the expected EnMAP calibration stability on the uncertainty in the ground reflectance product is investigated. Using a Monte-Carlo approach, the radiometric calibration stability and the spectral calibration stability are treated as sources of uncertainty which influence the ATCOR atmospheric correction and consequently the uncertainty related to the generated ground reflectance product. This uncertainty is estimated for the simulated EnMAP scene of Barrax, Spain.

Assuming a radiometric stability ±2.5% between two consecutive calibrations, the relative combined standard uncertainty in ground reflectance is ~2.5% for wavelength above 700 nm. For wavelength shorter than 700 nm, a general exponential increase towards shorter wavelength can be observed. Also, the uncertainty depends on the brightness of the ground cover class. Regarding the assumed EnMAP spectral stability of ±0.5 nm, the influence on the uncertainty in the ground reflectance product is less pronounced. The absolute magnitude of the combined standard uncertainty is well below 0.2% absolute reflectance for wavelengths outside atmospheric absorption regions, and ~0.7%–2.0% reflectance in the weaker atmospheric absorptions regions. For the ±2 nm shift scenario, the relative uncertainty is increased, being in the range of 4%–15% reflectance for wavelength regions affected by weak atmospheric absorption processes. Also, the exponential increase of uncertainty for wavelengths shorter than 700 nm is prominent.

When analysing the influence of the radiometric stability on the ATCOR estimations of the atmospheric conditions, the AOT as well as the WV retrieval clearly show an increase in uncertainty. For the radiometric case, the mean relative uncertainty of the AOT product is 9.6%, and is spatially variable over the scene. This is partly due to a significant change in the underlying identification of DDV pixels used for AOT retrieval. Also, regarding the WV retrieval, relative uncertainty in WV column is about 2.7%. As a consequence, the uncertainties of all products, ground reflectance, WV and AOT, are variable over the scene. For the spectral 0.5 nm shift scenario, only a small influence on the AOT and WV retrieval is observed. However, for the 2 nm shift scenario, again a significant influence on AOT and WV retrieval occurs resulting in a relative uncertainty of ~2.7% for the AOT and ~4% for the WV products. The observed increased uncertainty in the AOT retrieval causes the exponential increase in uncertainty in the ground reflectance products for wavelengths shorter than 700 nm, as this wavelength region is heavily influenced by aerosols, and an accurate correction is crucial.

The consequences for the higher-level thematic products are briefly illustrated by the uncertainty related to vegetation indices. The broad-band index NDVI is significantly affected by the radiometric stability showing a relative uncertainty of ~8%–9%, and is also slightly affected by spectral shifts (relative uncertainty <1.3% in case of 2 nm shifts, and <0.1% for 0.5 nm shifts). The small-band PRI index is affected even by small spectral shifts, having a relative uncertainty of 2% for 0.5 nm shifts, and ~12% for 2 nm shifts. For the radiometric case, a severe relative uncertainty of 63% is observed within the test scene. This can be explained as a consequence of the AOT-related exponentially increased uncertainty towards short wavelengths, as the PRI uses only bands below 570 nm.

To conclude, the finding of this uncertainty study underpin the relevance of data quality control procedures within the processing chain, instrument monitoring routines as well as independent vicarious validation activities. As in practice, many types of radiometric defects such as single de-calibrated bands can be easily identified by taking advantage of the high band-to-band correlation and thus redundancy which is inherent in hyperspectral data. Also, spectral shifts can be detected and corrected using the EnMAP on-board calibration sources as well as approaches based on well-defined atmospheric absorption features. These and other CalVal activities are therefore foreseen within the EnMAP mission ensuring a high data quality.

Acknowledgments

Author Contributions

Martin Bachmann, Aliaksei Makarau and Rudolf Richter conceived and designed the experiments; Martin Bachmann and Aliaksei Makarau performed the experiments; Martin Bachmann, Aliaksei Makarau, Rudolf Richter and Karl Segl analyzed the data; Karl Segl contributed materials; Martin Bachmann, Aliaksei Makarau, Rudolf Richter and Karl Segl wrote the paper.

Conflicts of Interest

The authors declare no conflict of interest.

References

1. QA4EO Task Team. A Quality Assurance Framework for Earth Observation: Principles. Available online: http://qa4eo.org/docs/QA4EO_Principles_v4.0.pdf (accessed on 28 May 2015).
2. Fox, N. A Guide to Expression of Uncertainty of Measurements. Available online: http://qa4eo.org/docs/QA4EO-QAEO-GEN-DQK-006_v4.0.pdf (accessed on 28 May 2015).
3. Evaluation of Measurement Data—Guide to the Expression of Uncertainty in Measurement. Available online: http://www.bim.government.bg/0/3D3F3380D3DB8BE2C22579000029F199/$FILE/JCGM_100_2008_E_GUM.pdf (accessed on 2 June 2015).
4. Bachmann, M.; Adar, S.; Ben-Dor, E.; Biesemans, J.; Briottet, X.; Grant, M.; Hanus, J.; Holzwarth, S.; Hueni, A.; Kneubuehler, M.; *et al*. Towards agreed data quality layers for airborne hyperspectral imagery. In Proceedings of the 7th EARSeL-SIG-IS, Edinburgh, UK, 11–13 April 2011.
5. Beekhuizen, J.; Bachmann, M.; Ben-Dor, J.; Biesemans, M.; Grant, G.; Heuvelink,G.; Hueni, A.; Kneubuehler, M.; de Miguel, E.; Pimstein, A.; *et al*. *Report on Full Error Propagation Concept*; European Comission EUFAR Office: Toulouse, France, 2009.
6. Woolliams, E.; Hueni, A.; Gorrono, J. Intermediate Uncertainty Analysis for Earth Observation (Instrument Calibration). NPL Training Course Textbook. Available online: http://www.emceoc.org/documents/uaeo-int-trg-course.pdf (accessed on 28 May 2015).
7. Schaepman, M.; Jehle, M.; Hueni, A.; D'Odorico, P.; Damm, A.; Weyermann, J.; Schneider, F.; Laurent, V.; Popp, C.; Seidel, F.; *et al*. Advanced radiometry measurements and Earth science applications with the Airborne Prism Experiment (APEX). *Remote Sens. Environ.* **2014**, *158*, 207–219.

8. Kerr, G.; Fischer, C.; Reulke, R. A blind-deconvolution approach for a data-driven estimation of image reflectance variability. *IEEE Trans. Geosci. Remote Sens.* **2015**, submitted.

9. Segl, K.; Guanter, L.; Kuester, T.; Roessner, R.; Kaufmann, H.; Sang, B.; Mogulsky, V.; Hofer, S. EeteS—The EnMAP end-to-end simulation tool. *IEEE J. Sel. Top. Appl. Earth Obs. Remote Sens.* **2012**, *5*, 522–530.

10. Storch, T.; Bachmann, M.; Honold, H.-P.; Kaufmann, H.; Krawczyk, H.; Müller, R.; Sang, B.; Schneider, M.; Segl, K.; Chlebek, C. EnMAP data product standards. In Proceedings of the Geoscience and Remote Sensing Symposium (IGARSS), Quebec, QC, Canada, 13–18 July 2014.

11. Richter, R.; Schläpfer, D. Geo-atmospheric processing of airborne imaging spectrometry data. Part 2: Atmospheric/topographic correction. *Int. J. Remote Sens.* **2002**, *23*, 2631–2649.

12. Stuffler, T.; Kaufmann, H.; Hofer, S.; Foerster, K.-P.; Schreier, G.; Mueller, A.; Eckardt, A.; Bach, H.; Penne, B.; Benz, U.; *et al.* The EnMAP hyperspectral imager—An advanced optical payload for future applications in earth observation programmes. *Acta Astronaut.* **2007**, *61*, 115–120.

13. Storch, T.; Bachmann, M.; Eberle, S.; Habermeyer, M.; Makasy, C.; de Miguel, A.; Mühle, H.; Müller, R. EnMAP ground segment design: An overview and its hyperspectral image processing chain. In *Earth Observation of Global Changes (EOGC)*; Springer-Verlag: Berlin, Germany; Heidelberg, Germany, 2013; pp. 49–62.

14. Guanter, L.; Kaufmann, H.; Segl, K.; Foerster, S.; Rogass, C.; Chabrillat, S.; Kuester, T.; Hollstein, A.; Rossner, G.; Chlebek, C.; *et al.* The Environmental Mapping and Analysis Program (EnMAP) spaceborne imaging spectroscopy mission for Earth observation. *Remote Sens.* **2015**, submitted.

15. Green, R.; Pavri, B.; Chrien, T. On-orbit radiometric and spectral calibration characteristics of EO-1 Hyperion derived with an underflight of AVIRIS and *in situ* measurements at Salar de Arizaro, Argentina. *IEEE Trans. Geosci. Remote Sens.* **2003**, *41*, 1194–1203.

16. Cocks, T.; Jensen, T.; Steward, A.; Wilson, I.; Schields, T. The HyMap airborne hyperspectral sensor: The system, calibration and performance. In Proceedings of the First EARSeL Workshop on Imaging Spectroscopy, Zürich, Switzerland, 6–8 October 1998.

17. Bachmann, M.; Habermayer, M.; Holzwarth, S.; Richter, R.; Müller, A. Including quality measures in an automated processing chain for airborne hyperspectral data. In Proceedings of the 5th EARSeL Workshop on Imaging Spectroscopy, Bruges, Belgium, 23–25 April 2007.

18. Guanter, L.; Richter, R.; Moreno, J. Spectral calibration of hyperspectral imagery using atmospheric absorption features. *Appl. Opt.* **2006**, *45*, 2360–2370.

19. Richter, R.; Schlapfer, D. ATCOR User Manual. Available online: www.rese.ch/pdf/atcor3_manual.pdf (accessed on 28 May 2015).

20. Berk, A.; Bernstein, L.; Anderson, G.; Acharay, P.; Robertson, D.; Chetwynd, J.; Adler-Golden, S. MODTRAN cloud and multiple scattering upgrades with application to AVIRIS. *Remote Sens. Environ.* **1998**, *65*, 367–375.

21. Richter, R. Correction of satellite imagery over mountainous terrain. *Appl. Opt.* **1998**, *37*, 4004–4015.

22. Kaufman, Y.; Wald, A.; Remer, L.; Gao, B.-C.; Li, R.-R.; Flynn, L. The MODIS 2.1 μm channel—Correlation with visible reflectance for use in remote sensing of aerosol. *IEEE Trans. Geosci. Remote Sens.* **1997**, *35*, 1286–1298.

23. Schläpfer, D.; Borel, C.; Keller, J.; Itten, K. Atmospheric precorrected differential absorption technique to retrieve columnar water vapor. *Remote Sens. Environ.* **1998**, *65*, 353–366.

24. Richter, R.; Schläpfer, D. Considerations on water vapor and surface reflectance retrievals for a spaceborne imaging spectrometer. *IEEE Trans. Geosci. Remote Sens.* **2008**, *46*, 1958–1966.

25. Richter, R.; Wang, X.; Bachmann, M.; Schläpfer, D. Correction of cirrus effects in Sentinel-2 type of imagery. *Int. J. Remote Sens.* **2011**, *32*, 2931–2941.

26. Richter, R.; Schläpfer, D.; Müller, A. Operational atmospheric correction for imaging spectrometers accounting for the smile effect. *IEEE Trans. Geosci. Remote Sens.* **2011**, *49*, 1772–1780.

27. Segl, K.; Guanter, L.; Kaufmann, H. Simulation of spatial sensor characteristics in the context of the EnMAP hyperspectral mission. *IEEE Trans. Geosci. Remote Sens.* **2010**, *48*, 3046–3054.

28. Guanter, L.; Segl, K.; Kaufmann, H. Simulation of optical remote sensing scenes with application to the EnMAP hyperspectral mission. *IEEE Trans. Geosci. Remote Sens.* **2009**, *47*, 2340–2351.

29. European Space Agency. ESA Earth Observation Campaigns Data. Avaliable online: https://earth.esa.int/web/guest/campaigns (accessed on 28 May 2015).

30. Verhoef, W.; Bach, H. Coupled soil-Leaf-Canopy and atmosphere radiative transfer modeling to simulate hyperspectral multi-angular surface reflectance and TOA radiance data. *Remote Sens. Environ.* **2007**, *109*, 166–182.

31. Press, W.; Teukolsky, S.; Vetterling, W.; Flannery, B. *Numerical Recipes in C. The Art of Scientific Computing*, 2nd ed.; Cambridge University Press: New York, NY, USA, 1992.

32. Garbulsky, M.; Peñuelas, J.; Gamon, J.; Inoue, Y.; Filella, I. The photochemical reflectance index (PRI) and the remote sensing of leaf, canopy and ecosystem radiation use efficiencies: A review and meta-analysis. *Remote Sens. Environ.* **2011**, *115*, 281–297.

33. Suárez, L.; Zarco-Tejada, P.; Sepulcre-Cantó, G.; Pérez-Priego, O.; Miller, J.; Jiménez-Muñoz, J.; Sobrino, J. Assessing canopy PRI for water stress detection with diurnal airborne imagery. *Remote Sens. Environ.* **2008**, *112*, 560–575.

34. Mõttus, M.; Takala, T.; Stenberg, P.; Knyazikhin, Y.; Yang, B.; Nilson, T. Diffuse sky radiation influences the relationship between canopy PRI and shadow fraction. *ISPRS J. Photogramm. Remote Sens.* **2015**, *105*, 54–60.